coatings

MDPI

Communication

Surface Modification of Hydroxyapatite Coating for Enhanced Antibiotic Therapy

Rongrong Jia [1,2], Kai Li [2,3,*], Jieping Li [2,3], Deliang Yi [2,3], Yi Ding [2], Guangzhi Yang [1,*] and Xuebin Zheng [2,3,*]

[1] School of Materials and Chemistry, University of Shanghai for Science and Technology, 516 Jungong Road, Shanghai 200095, China; rrjia_13164377675@163.com
[2] Key Laboratory of Inorganic Coating Materials CAS, Shanghai Institute of Ceramics, Chinese Academy of Sciences, 1295 Dingxi Road, Shanghai 200050, China; lijieping20@mails.ucas.ac.cn (J.L.); yideliang@mail.sic.ac.cn (D.Y.); dingyi@mail.sic.ac.cn (Y.D.)
[3] Center of Materials Science and Optoelectronics Engineering, University of Chinese Academy of Sciences, 19 Yuquan Road, Beijing 100049, China
* Correspondence: likai@mail.sic.ac.cn (K.L.); yanggzh@usst.edu.cn (G.Y.); xbzheng@mail.sic.ac.cn (X.Z.)

Abstract: A major strategy to combat implant-associated infections is to develop implant coatings with intrinsic antibacterial activity. Since hydroxyapatite (HAp) coatings and antibiotic administration are commonly used in clinical settings, developing HAp-coated implants with localized antibiotic-releasing properties has attracted popularity. Considering the antibacterial metal species (Ag, Zn, Cu, etc.) in metal–organic frameworks and their drug delivery capacity, in this study, a gentamicin-loaded zeolitic imidazolate framework-8 nanolayer was deposited on a plasma-sprayed HAp coating (HAp/ZIF-8@Gent), which served as a Gent and Zn^{2+} reservoir. The investigation on the binding interaction between ZIF-8 and HAp indicated that the growth of ZIF-8 was through a Zn^{2+} seed layer on the HAp coating via an adsorption–replacement mechanism, instead of simple physical adsorption. The HAp/ZIF-8@Gent coating exhibited a sustained drug-release property, and the cumulative concentration of released Gent reached 239.8 ± 7.1 μg/mL on day 8. Compared to the HAp-Zn and HAp/ZIF-8 coatings, the HAp/ZIF-8@Gent coating exhibited significantly higher antibacterial activity against *E. coli*. This was ascribed to the combined antibacterial effects of Zn^{2+} and Gent. The cytocompatibility of the HAp/ZIF-8@Gent coating was confirmed via cell proliferation. Above all, the ZIF-8-modified HAp coating with localized delivery of Gent and Zn^{2+} possessed excellent antibacterial activity and acceptable cytocompatibility, showing potential in mitigating implant-associated infections.

Keywords: hydroxyapatite; gentamicin; ZIF-8; Zn^{2+}; antibacterial activity

Citation: Jia, R.; Li, K.; Li, J.; Yi, D.; Ding, Y.; Yang, G.; Zheng, X. Surface Modification of Hydroxyapatite Coating for Enhanced Antibiotic Therapy. *Coatings* **2024**, *14*, 477. https://doi.org/10.3390/coatings14040477

Academic Editor: Alina Vladescu

Received: 7 March 2024
Revised: 5 April 2024
Accepted: 11 April 2024
Published: 13 April 2024

1. Introduction

Titanium (Ti) and its alloys have found extensive applications as metallic bone implants [1], attributed to their remarkable mechanical properties and biocompatibility [2–4]. In order to enhance the fixation of Ti-based implants to bone, hydroxyapatite (HAp) coatings are fabricated on the implant surfaces in clinical settings as HAp constitutes the inorganic composition of natural bone [5–8]. Although HAp-coated implants have achieved successful applications in the past several decades, implant-associated infections (IAIs) which result from bacterial adhesion and biofilm formation seriously impair clinical outcomes of implants [9–11]. Nowadays, IAIs are considered to be one of the most prevalent and intricate hurdles in orthopedic [12]. In order to combat IAIs, current medical techniques mainly involve systemic antibiotic treatments [13]. However, higher-concentration antibiotics must be administered to maintain sufficient drug concentration at the lesion site. In the past, the antibacterial use of hydroxyapatite doped with transition metal elements (Ag, Zn, Cu, etc.) has been widely studied [14–16]. However, in order to improve its biocompatibility, it will inevitably lead to a decrease in antibacterial activity. To mitigate these

challenges, developing HAp-coated implants with localized antibiotic-releasing properties has attracted popularity.

Metal–organic frameworks (MOFs), considering their high surface area and tunable composition, exhibit a range of potential applications in drug delivery and catalysis support [17–19]. As a member of the MOF family, zeolitic imidazolate framework-8 (ZIF-8), comprising Zn^{2+} ions and 2-methylimidazole ligands, possesses a crystalline topology similar to that of zeolites [17,20,21]. A recent work by Taheri and colleagues demonstrated that the released Zn^{2+} from the degradation of ZIF-8 endowed ZIF-8 with antibacterial activity. ZIF-8 has a higher degradation rate in phosphate buffer saline, resulting in stronger antibacterial activity even than antimicrobial agent ZnO [20]. The remarkable thermal stability and biodegradability of ZIF-8 endow it with potential in drug delivery [18]. For instance, ZIF-8 nanoparticles can serve as a carrier for various antibacterial and antitumor agents, enhancing drug loading capacity and extending drug release duration [19,22,23]. However, it is worth noting that previous studies have predominantly focused on the research of ZIF-8 nanoparticles. The utilization of ZIF-8 as a drug carrier on orthopedic implants remains unexplored. Due to the metal ion adsorption properties of ZIF-8 and HAp, previous studies have combined ZIF-8 with HAp particles as an absorbent in the removal of metallic pollutants in waste water [24,25]. The surface of HAp is saturated with negatively charged PO_4^{3-}, which is able to absorb metal cations (Zn^{2+}, Pb^{2+}, Cd^{2+} etc.) through an adsorption–replacement mechanism [26–28]. Thus, the introduction of a Zn^{2+} seed layer on HAp can facilitate the nucleation and in situ growth of ZIF-8 crystal.

In this study, ZIF-8 nanolayer was deposited on a plasma-sprayed HAp coating (HAp/ZIF-8) via a facile "one-pot" method. The binding interaction between ZIF-8 and HAp was investigated via XRD, Raman, and XPS analysis. A gentamicin-loaded HAp/ZIF-8 (HAp/ZIF-8@Gent) coating was employed to investigate the combined antibacterial effects of Zn^{2+} and Gent against *E. coli*. The ZIF-8 modified, Zn^{2+}-absorbed, and pure HAp coatings served as controls. The cytocompatibility of the HAp/ZIF-8@Gent coating was evaluated by measuring osteoblastic cell proliferation.

2. Materials and Methods

2.1. Coating Preparation

Utilizing the vacuum plasma spraying system (F4-VB, Sulzer Metco, Winterthur, Switzerland), a hydroxyapatite (HAp, CAM Bioceramics, Leiden, Netherlands) coating was prepared on a Ti-6Al-4V substrate (Ø10 mm × 2 mm, Shenyang Zhonghang Titanium Co., Shenyang, China) [29]. Initially, 0.7435 g of Zn $(NO_3)_2 \cdot 6H_2O$ (99.99%, Sinopharm Chemical Reagent Co., Shanghai, China) was dissolved in 50 mL of deionized water, yielding solution A. Subsequently, the plasma-sprayed HAp coating was immersed in solution A and stirred magnetically for 30 min, resulting in the formation of an HAp-Zn coating. Following this, 0.4105 g of 2-methylimidazole (≥98%, Titan Technology Co., Ltd., Shanghai, China) was dissolved in 50 mL of deionized water to obtain solution B. Solution B was then slowly introduced into solution A, and under ambient conditions, the mixture was stirred for 4 h, giving rise to the precursor coating. To facilitate the secondary growth of ZIF-8 on the coating surface, the precursor coating underwent immersion in a mixed solution comprising deionized water, Zn $(NO_3)_2$ $6H_2O$, and 2-methylimidazole for a duration of 4 h. Following this immersion, the coating was rinsed multiple times with pure water and dried. Consequently, the HAp/ZIF-8 coating was successfully obtained.

The procedures for fabricating the HAp/ZIF-8@Gent coating closely parallel those for the HAp/ZIF-8 coating, with the exception of a slight modification to solution B during the preparation. Specifically, gentamicin sulfate (Gent, Titan Technology Co., Ltd., Shanghai, China) was introduced into the 2-methylimidazole solution at a concentration of 5 mg/mL.

2.2. Surface Characterization

Employing the grazing incidence diffraction mode of an X-ray diffractometer (XRD, D8 Discover Davinci, Bruker Corporation, Rheinstetten, Germany), the characterization

analysis of the phase composition of the coating was conducted. Furthermore, the analysis of the organic chemical components on the surface of the coating was performed using the in situ laser Raman spectrometer (Raman, in Via, Renishaw, United Kingdom), and the Fourier infrared spectrometer (FTIR, Spotlight400, PerkinElmer Corporation, Waltham, MA, USA) The surface morphological features of the coating were examined using a field emission scanning electron Microscope (FE-SEM, Magellan 400, FEI Corporation, Hillsboro, OR, USA), along with energy spectrum analysis. Additionally, the component analysis of the coating's surface was carried out through X-ray photoelectron spectroscopy (XPS, Escalab 250Xi, Thermo Fisher Scientific, Waltham, MA, USA).

2.3. Establishment of the Calibration Curve

The characterization of Gent solution at various concentrations (10–150 μg/mL) in phosphate buffer solution was performed using a UV–Visible spectrophotometer (UV–Vis, UV-4100, Metashi, Shanghai, China). The wavelength, λmax, corresponding to the highest peak was selected, and the function relating the absorbance intensity to the concentration of Gent was recorded. Subsequently, a standard curve was generated from these data and utilized for subsequent experiments. Each experiment was conducted thrice, yielding an average value and standard deviation.

2.4. In Vitro Drug Release

The linear relationship was established as a standard curve between absorbance (A) and Gent concentration (C) at the maximum peak-absorption wave length (256 nm). To assess the temporal evolution of gentamicin (Gent) release from HAp/ZIF-8@Gent coatings, the coatings were immersed in 4 mL of PBS buffer solution (pH 7.4) and incubated at 37 °C in a constant-temperature chamber. At specific time intervals, 1 mL of PBS sample was extracted to ascertain the release kinetics, with an equivalent volume of fresh PBS replenished after each sampling. Sample collection was conducted at 30 min, 1 h, 2 h, 4 h, 8 h, 24 h, 48 h, 5 days, and 8 days, followed by Gent release calculations based on a standard curve.

2.5. In Vitro Antibacterial Testing

The antibacterial efficacy of four types of coatings, namely, HAp, HAp-Zn, HAp/ZIF-8, and HAp/ZIF-8@Gent, was evaluated using the agar diffusion method. The samples were grouped and placed in disposable glass dishes, undergoing dual-sided ultraviolet sterilization for 30 min as preparation. Sterile PBS solution was employed to dilute *E. coli* bacterial suspension to a concentration of 10^5 CFU/mL. Subsequently, 100 μL of the diluted suspension was evenly spread onto LB culture medium (Haibo Biotechnology, Qingdao, China). Post-sterilization, the coated samples were individually positioned onto the culture medium, lightly pressed with sterile forceps to ensure optimal contact between the samples and the medium. The petri dishes were then placed in a constant-temperature incubator set at 37 °C for 24 h. Upon completion of the incubation, the dishes were retrieved and subjected to photography using a standard camera, with the measurement and recording of the sizes of the inhibition zones.

The antibacterial efficacy of the four coatings was evaluated using the plate counting method. *E. coli* bacterial suspensions were diluted to a concentration of 10^5 CFU/mL in LB liquid culture medium. Subsequently, 20 μL of the diluted bacterial suspension was added to the surface of each sample. The samples were then placed in a constant-temperature incubator set at 37 °C for static cultivation of 24 h. Then, 980 μL PBS was used to wash a sample. The bacterial suspension was subjected to ten-fold dilution using PBS, and 100 μL of the diluted suspension was uniformly spread onto LB solid culture medium. Subsequently, the Petri dishes were positioned in a constant-temperature incubator set at 37 °C for 18 h. The dishes were retrieved for photography, and the bacterial colony counts were recorded.

The antibacterial efficacy (%) can be calculated using the following formula:

Antibacterial Efficacy (%) = (1 − Experimental Group Bacterial Concentration/Control Group Bacterial Concentration) × 100%.

2.6. Cell Culture

The murine pre-osteoblastic cell line MC3T3-E1 (purchased from the Cell Bank of the Chinese Academy of Sciences) was cultured in α-MEM (Hyclone, Logan, UT, USA) supplemented with 10% fetal bovine serum (Wisent, Nanjing, China). The cells were cultured in a CO_2 incubator at 37 °C with medium replacement every two days.

2.7. Cell Proliferation Assay

The proliferative behavior of MC3T3-E1 cells on the surfaces of the four coating materials was assessed using the CCK-8 kit (Tongren institute of chemistry, Kyushu Island, Japan). Each aseptic material was placed carefully in a 48-well cell culture plate. Well-growing MC3T3-E1 cells were collected and digested, and the cell suspension concentration was adjusted. A volume of 100 μL of cell suspension (containing 10^4 cells/mL) was seeded onto the surface of each material in the wells and allowed to sit for 3–4 h, with a normal control group established. After the cells adhered to the sample, we added culture medium. The cells were cultured in a CO_2 incubator at 37 °C for 1, 4, and 7 days. After the incubation period, the culture medium was discarded from each well. Subsequently, 1 mL of fresh culture medium and 0.1 mL of CCK-8 solution were added to each well. The cells were further incubated at 37 °C in a 5% CO_2 cell culture incubator for an additional 2–3 h. Carefully, the solution from each well was aspirated and transferred to a 96-well plate. The optical density (OD) values of each well were measured at 450 nm using a microplate (Multiskan Spectrum, Thermo Fisher Scientific, Waltham, MA, USA) reader.

2.8. Statistical Analysis

The data are presented as the mean ± standard deviation (SD) from three parallel experiments. Statistical analysis was conducted using GraphPad Prism 8.0 software, employing one-way analysis of variance (ANOVA) followed by Tukey's post hoc test for pairwise comparisons. Significance levels are denoted by * ($p < 0.05$), ** ($p < 0.01$), and *** ($p < 0.001$).

3. Results

3.1. Coating Characterization

Figure 1A shows the SEM images of as-prepared HAp, HAp/ZIF-8, and HAp/ZIF-8@Gent coatings. The surface of the HAp coating exhibited typical microstructure features of plasma-sprayed coating, which was built up of molten and semi-molten droplets. Compared to the HAp coating surface, the successful growth of nanoparticles was observed on the surfaces of both HAp/ZIF-8 and HAp/ZIF-8@Gent coatings. As shown in Figure 1B, in addition to Ca, P, and O elements, the presence of Zn and C elements was observed in HAp/ZIF-8. The percentage content of each element in the coating is shown in Table 1. These findings affirm the successful loading of ZIF-8 nanoparticles onto the surface of hydroxyapatite (HAp).

Table 1. The percentage of each element content in HAp/ZIF-8 coating.

Element	Weight%	Atomic%
Ca	19.06	9.31
P	13.75	8.69
O	48.03	58.73
Zn	5.97	1.79
C	13.19	21.49

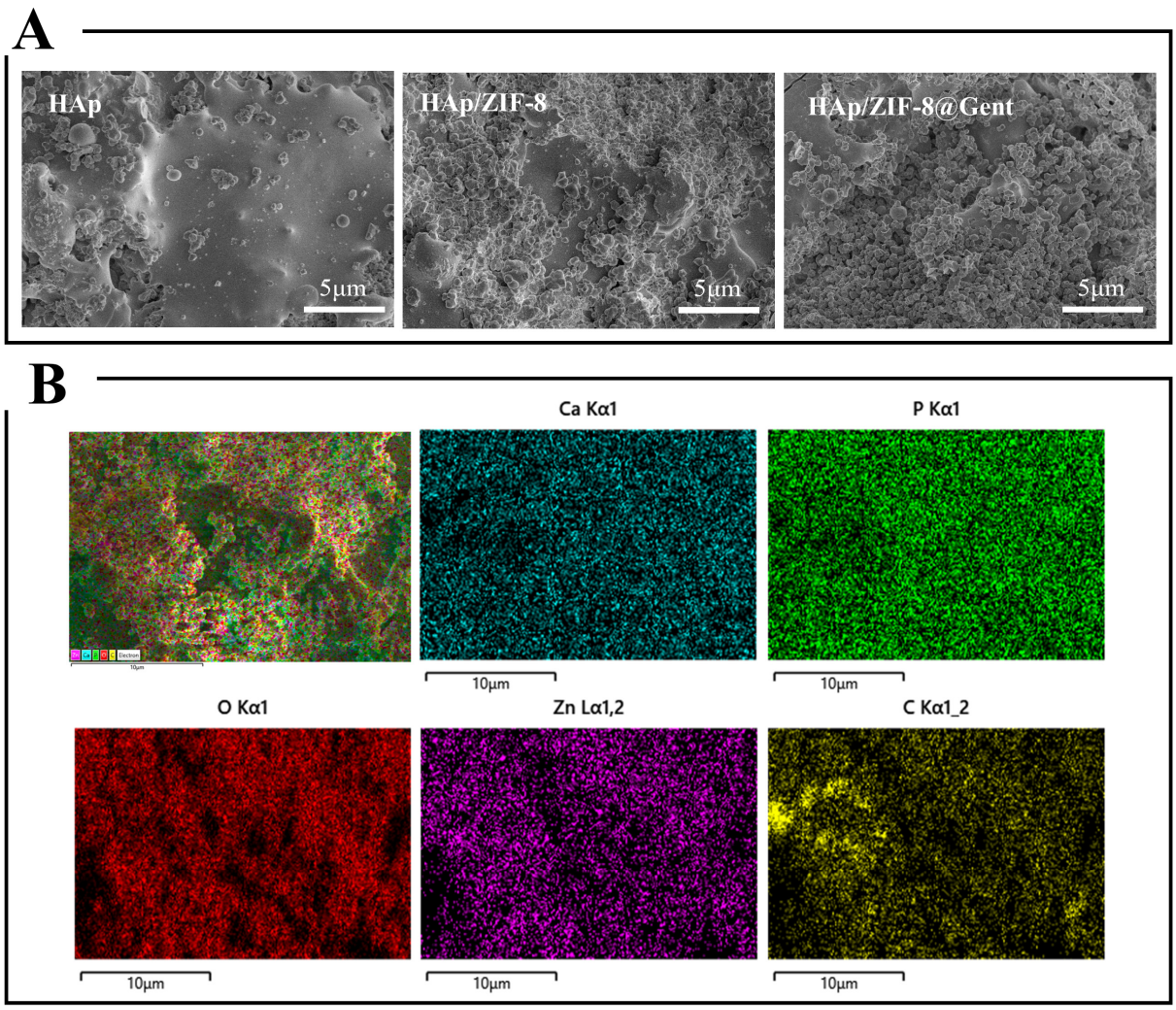

Figure 1. (**A**) SEM images of HAp, HAp/ZIF-8, and HAp/ZIF-8@Gent coatings. (**B**) Elemental distribution maps of the HAp/ZIF-8 coating surface.

The XRD patterns of the HAp, HAp/ZIF-8, and HAp/ZIF-8@Gent coatings are illustrated in Figure 2A. The distinctive peaks of HAp were observed for the three coatings. Specifically, the diffraction peaks at 2θ = 25.8°, 31.7°, 32.8°, 34.0°, and 39.7° correspond to the (002), (211), (300), (202), and (130) crystal planes of hydroxyapatite (PDF#74-566), respectively. The incorporation of ZIF-8 or ZIF-8@Gent did not induce significant alterations in the crystalline structure of the underlying hydroxyapatite (HAp).

Further FTIR analysis was conducted, as shown in Figure 2B. In the spectrum of Gent, it can be observed that the bands at 1640 cm^{-1} and 1532 cm^{-1} were N-H shear vibration absorption bands [30,31]. Moreover, a distinct absorption band was evident in the range of 900 to 1300 cm^{-1}, corresponding to the stretching vibrations of C-N and C-O groups [32]. Compared to HAp, HAp/ZIF-8 exhibited increased peak intensity in the wavenumber range of 900 to 1300 cm^{-1}, which was ascribed to the stretching vibrations of C-N groups of ZIF-8 [33,34]. Meanwhile, the FTIR spectrum of the HAp/ZIF-8@Gent coating exhibited a notable augmentation in both the intensity and width of the absorption peaks within the wavenumber range of 900 to 1300 cm^{-1} and 525 to 630 cm^{-1}, indicating the successful loading of Gent within the coating.

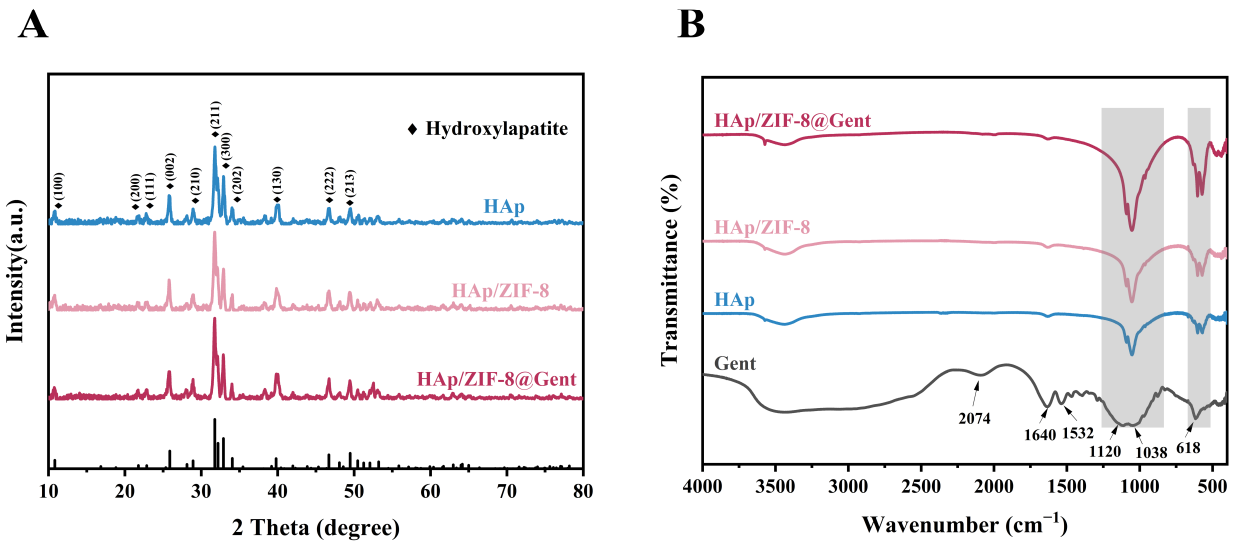

Figure 2. (**A**) XRD patterns and (**B**) FTIR spectra of HAp, HAp/ZIF-8, and HAp/ZIF-8@Gent coatings.

3.2. Binding Interactions between ZIF-8 and HAp

To investigate the binding mode between ZIF-8 nanoparticles and HAp coating, a Zn^{2+}-absorbed HAp (HAp-Zn) coating was prepared. The XRD patterns of the HAp-Zn and HAp coatings are shown in Figure 3A. The diffraction peak intensity of HAp-Zn was slightly reduced compared to that of HAp. This phenomenon may be attributed to the exchange of Zn^{2+} with Ca^{2+} in HAp, thereby influencing the atomic positions or atomic density within the crystal lattice [35]. Interestingly, after loading with Zn^{2+}, the diffraction peak of the (211) crystal plane in HAp-Zn shifted to a higher 2θ value (Figure 3B). Moreover, the unit cell parameters of HAp-Zn were found to decrease compared to those of HAp (Table 2). This phenomenon arose from the ion exchange of Ca^{2+} by Zn^{2+}, considering the smaller ionic radius of Zn^{2+} (0.74 Å) than that of Ca^{2+} (0.99 Å) [36,37]. The Raman spectra of the HAp and HAp-Zn coatings are shown in Figure 3C. The peak at 961 cm^{-1} for the HAp coating corresponded to the symmetric stretching vibrations of P-O in PO_4^{3-} [38]. In contrast, the peak intensity in the HAp-Zn coating was decreased and the width of the peak was broadened. These indicated that Zn^{2+} occupied the HAp lattice through ion exchange reactions. XPS spectra of HAp and HAp-Zn coatings were also analyzed to investigate the interaction between Zn^{2+} and HAp (Figure 3D). In the spectrum of HAp-Zn, peaks corresponding to the Zn 2p orbitals were detected at 1022.1 eV and 1045 eV. Moreover, there was a slight shift and weakening of Ca and P peaks in HAp-Zn compared to HAp.

Table 2. Unit cell parameters of HAp and HAp-Zn.

Sample	Unit Cell Parameters (Å)	
	a	c
HAp (PDF#74-566)	9.424	6.879
HAp	9.419	6.896
HAp-Zn	9.377	6.895

HAp has excellent metal ion adsorption properties [6,36], and its adsorption mechanisms include (i) a dissolution–precipitation mechanism, which means that HAp first dissolves phosphate and then combines with metal ions; and (ii) an adsorption–replacement mechanism, whereby metal ions are first adsorbed on the surface of hydroxyapatite and then replace Ca^{2+}. Based on the above results, it is suggested that HAp-Zn predominantly involved an adsorption–replacement mechanism, further facilitating the heteronucleation of ZIF-8 crystals on the surface of HAp.

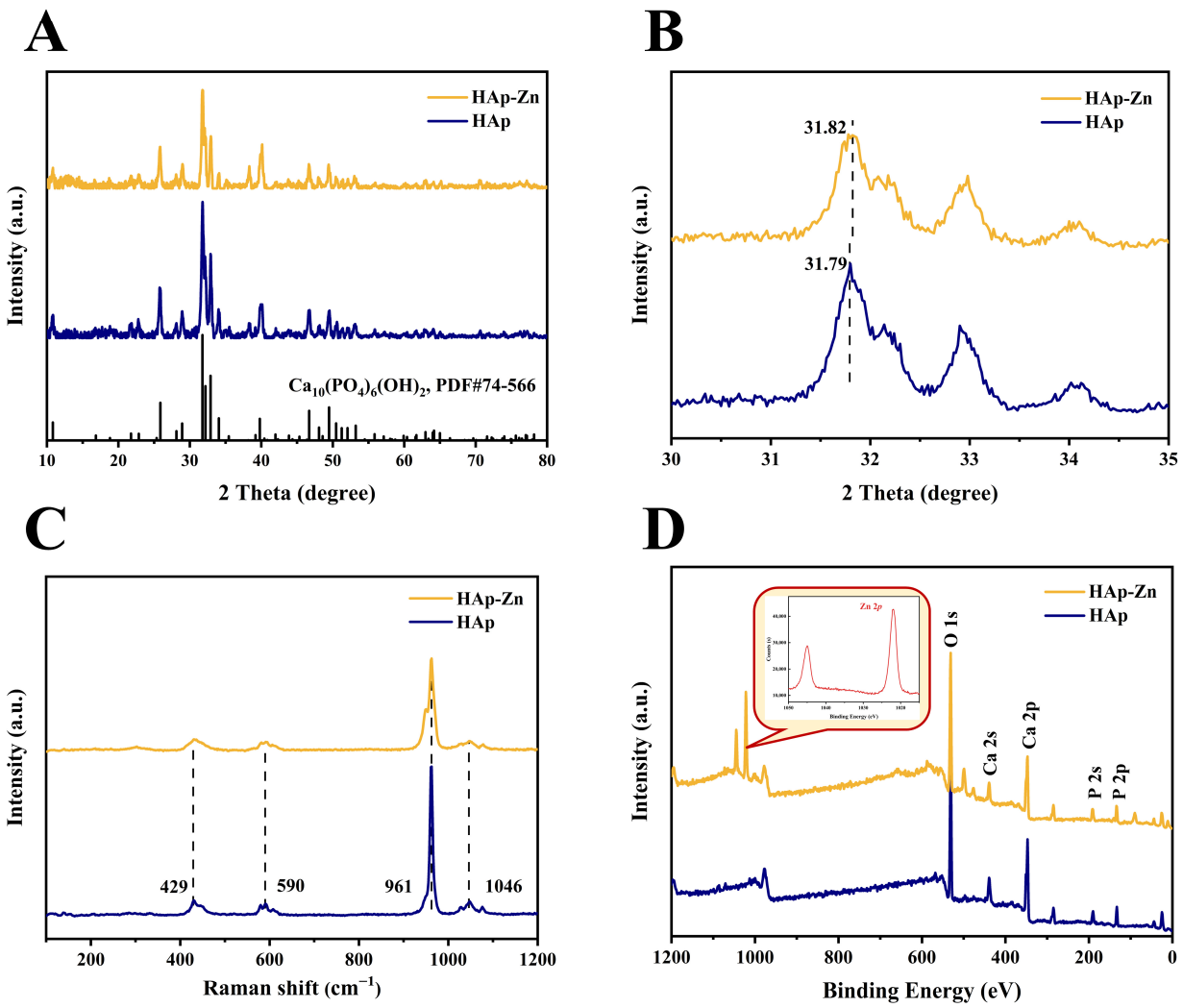

Figure 3. (**A**) XRD patterns. (**B**) Enlarged 2θ range of 30–35° of XRD patterns. (**C**) Raman spectra. (**D**) XPS spectra of the HAp and HAp-Zn coatings.

3.3. Drug Release Behavior of HAp/ZIF-8@Gent Coatings

As depicted in Figure 4A, the cumulative release rate of Gent in HAp/ZIF-8@Gent coatings gradually increased with the soaking time. In the initial 4 h, the total content of drug release reached 38.5%. The initial burst-released drug was mainly from the adsorbed drug on the HAp surface. Subsequently, the drug release rate markedly decelerated. This was probably because the ZIF-8 nanolayer, as a drug carrier, allowed for the sustained release of Gent. The drug release extended to 8 days. This might fulfill the antibacterial requirement for orthopedic implants in clinical settings that antibiotic release within 1–2 weeks can effectively prevent bacterial infection.

The cumulatively released Gent concentration is shown in Figure 4B. The drug concentration achieved 92.3 μg/mL within 4 h and reached equilibrium on the eighth day with a maximal value of 239.8 ± 7.1 μg/mL. The released Gent concentration in our study fell within the range of effective antibacterial concentration as reported previously. In the work by Zhang et al. [39], Gent was covalently grafted into the sodium alginate layer on the Ti implant surface, which also reached a concentration of approximately 87 μg/mL within 4 h. The coated Ti implant exhibited an in vitro and in vivo anti-infection ability. Nishtha Gaur et al. [40] utilized cold atmospheric plasma (CAP) to trigger the release of Gent from sodium polyacrylate particles in a hydrogel matrix. By activating using CAP for 2 min, the released concentration of Gent reached 65 μg/mL, which could effectively eradicate bacteria both in the planktonic state and within biofilms.

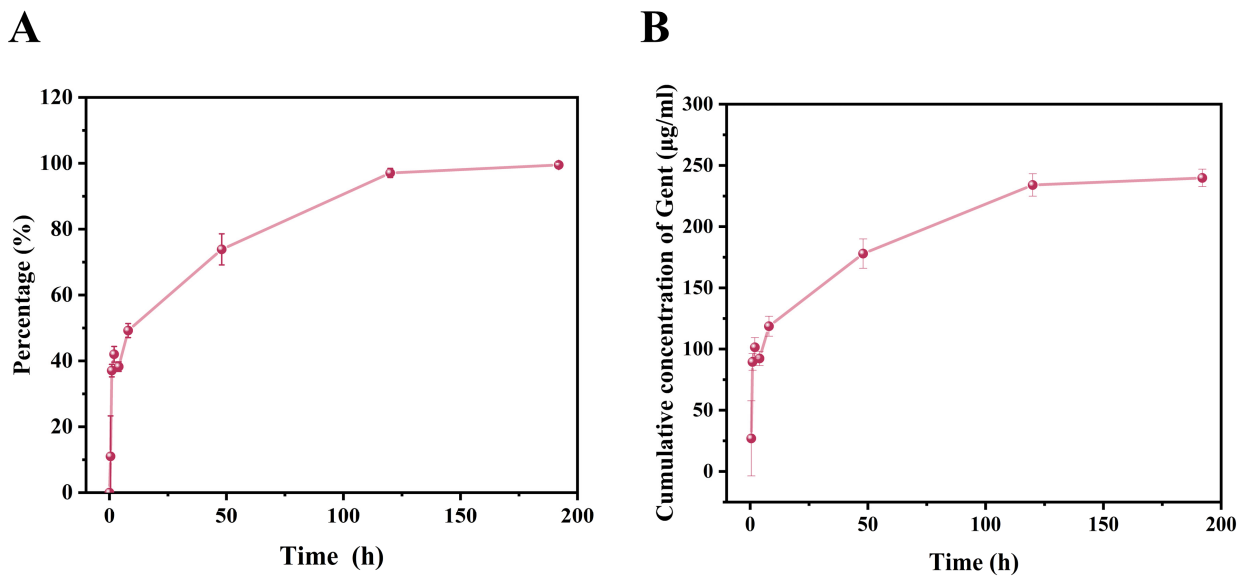

Figure 4. (**A**) The cumulative release rate of Gent in HAp/ZIF-8@Gent coating. (**B**) The cumulative release concentration of Gent.

3.4. In Vitro Antibacterial Activity

The in vitro antibacterial efficacy of the coatings against Gram-negative *E. coli* was assessed through the classical plate count method and the disc diffusion assay. The results of bacterial colony counting are shown in Figure 5A. For the HAp coating, a significant number of colonies was observed. In contrast, HAp-Zn and HAp/ZIF-8 coatings significantly inhibited the formation of colonies with HAp/ZIF-8 showing greater effect. Moreover, there were almost no colonies for the HAp/ZIF-8@Gent coating. The antibacterial efficiency of the HAp-Zn, HAp/ZIF-8, and HAp/ZIF-8@Gent coatings was 38.65%, 81.16%, and 99.99%, respectively.

Zn constitutes a pivotal trace element within the human body, exerting significant roles in immune regulation, prevention of cellular apoptosis, and bone metabolism [41]. According to antecedent research reports, elevated concentrations of Zn^{2+} manifest outstanding antibacterial and anti-inflammatory characteristics [41–43]. The principal antibacterial mechanisms include disruption of intracellular homeostasis, augmentation of bacterial membrane permeability, and bacterial polysaccharide synthesis [41,44]. The antibacterial effect of the HAp-Zn coating was mainly ascribed to the released Zn^{2+}. In contrast, the HAp/ZIF-8 coating with higher Zn^{2+} release exhibited higher antibacterial efficiency than the HAp-Zn coating. With the combined antibacterial effects of Zn^{2+} and Gent, the HAp/ZIF-8@Gent coating possessed the highest antibacterial efficiency. Gent is an aminoglycoside broad-spectrum antibiotic widely employed in the treatment of severe infections [45,46]. Its primary mode of action involves electrostatic binding with negatively charged phospholipid head groups, thereby impeding bacterial protein synthesis. Subsequently, Gent forms non-specific complexes by binding with specific ribosomal proteins, inducing the formation of non-specific complexes, consequently leading to mRNA misreading [46,47].

The results of the antibacterial zone experiment are presented in Figure 5B. It was clear that a noticeable antibacterial zone was observed around the HAp/ZIF-8@Gent coating, while no antibacterial zone was observed for the HAp, HAp-Zn, and HAp/ZIF-8 coatings. These outcomes may be attributed to the close adherence of the coating to the surface of the culture medium during testing, thereby suppressing the leaching of Zn^{2+} and consequently hindering its antibacterial efficacy. In contrast, the surface of the HAp/ZIF-8@Gent specimens featured water-soluble Gent, facilitating the dissolution of Gent and thus enabling an efficacious antibacterial effect.

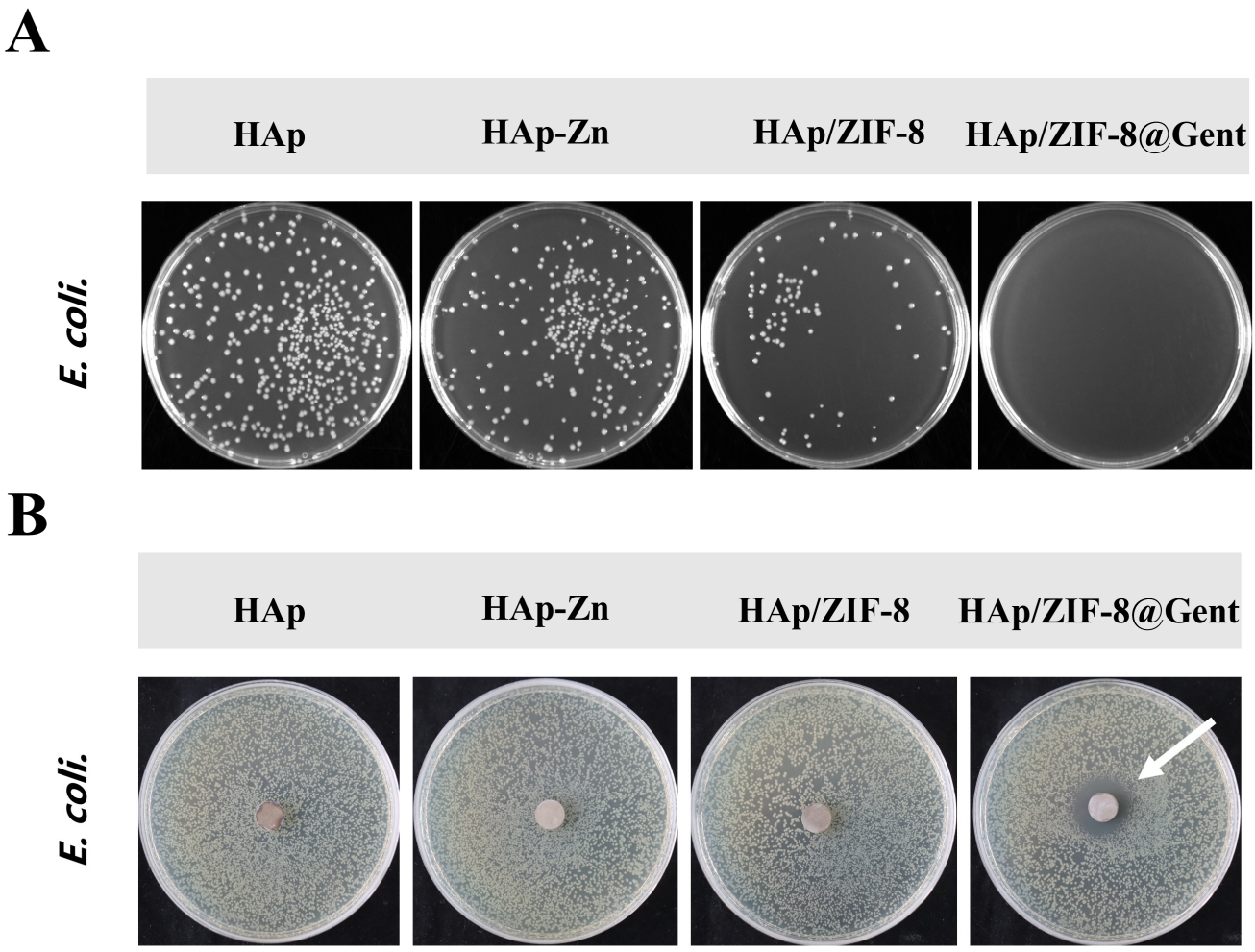

Figure 5. (**A**) Photos of *E. coli* colonies on the surface of the HAp, HAp-Zn, HAp/ZIF-8, and HAp/ZIF-8@Gent coatings. (**B**) Photos of inhibition zone experiments for the HAp, HAp-Zn, HAp/ZIF-8, and HAp/ZIF-8@Gent coatings.

3.5. Cytocompatibility of the Coatings

MC3T3-E1 cells were cultured on the surfaces of HAp, HAp-Zn, HAp/ZIF-8, and HAp/ZIF-8@Gent coatings for 1, 4, and 7 days, and the results of cell proliferation activity are shown in Figure 6. Observation reveals a continual proliferation of osteoblasts on the surfaces of all samples over the entire culture period. However, the HAp-Zn, HAp/ZIF-8, and HAp/ZIF-8@Gent coatings showed lower levels of cell proliferation than the HAp coating. The inhibitory effect on cell proliferation was the most pronounced on day 4 but was relieved on day 7. Considering that the HAp/ZIF-8@Gent coating showed a lower level of cell proliferation than the HAp/ZIF-8 coating, this indicated that the inhibitory effect was ascribed to the released Zn^{2+} and Gent from the coating surface [48]. Upon surpassing the zinc tolerance threshold in biological cells, cytotoxic responses are triggered [49]. Literature reviews have explored that within the concentration range of 1 to 100 μM, Zn^{2+} demonstrates effective antibacterial properties without inducing cytotoxic effects [50]. It was worth mentioning that the relative cellular viability of the HAp, HAp-Zn, HAp/ZIF-8, and HAp/ZIF-8@Gent coatings surpassed 70% that of the control. In accordance with ISO 10993.5 standards [51], cellular viability exceeding 70% [in comparison to the control group (cells inoculated in culture wells)] is deemed indicative of non-cytotoxicity. Pursuant to said standards, HAp, HAp-Zn, HAp/ZIF-8, and HAp/ZIF-8@Gent demonstrated non-cytotoxicity at 1 day, 4 days, and 7 days. This indicated that the HAp, HAp-Zn, HAp/ZIF-8, and HAp/ZIF-8@Gent coatings exhibited acceptable cytocompatibility.

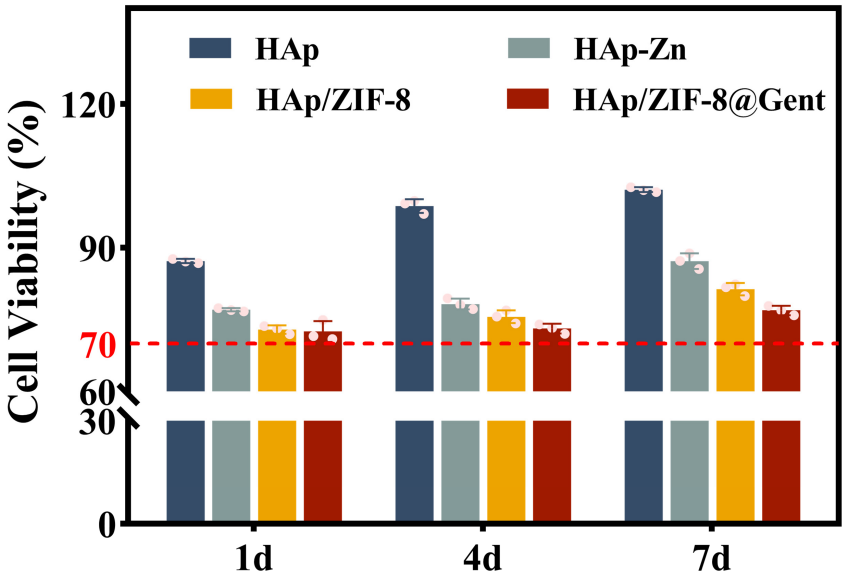

Figure 6. Viability of MC3T3-E1 cells on HAp, HAp-Zn, HAp/ZIF-8, and HAp/ZIF-8@Gent coating surfaces.

In our study, the incorporation of Gent into the ZIF-8 deposited on the coating surface can further augment the antibacterial efficacy of the composite coating. The synergistic antibacterial effects between ZIF-8 nanoparticles and Gent prove efficacious in eradicating Gram-negative bacteria. The aforementioned outcomes underscore that HAp/ZIF-8@Gent not only exhibits outstanding antibacterial prowess but also demonstrates commendable biocompatibility.

4. Conclusions

In this study, we employed a facial "one-pot" approach to synthesize a ZIF-8 nanolayer on a HAp coating surface, which served as Gent and Zn^{2+} reservoir. The binding interaction between ZIF-8 and HAp involved an adsorption–replacement mechanism, whereby Zn^{2+} ions were first adsorbed on the HAp surface and then replaced Ca^{2+} ions in HAp. The HAp/ZIF-8@Gent coating displayed a sustained drug-release property, and the released Gent concentration within 8 days fell in the range of effective antibacterial concentration as reported previously. Furthermore, the HAp/ZIF-8@Gent coating exhibited a higher antibacterial effect than the HAp-Zn and HAp/ZIF-8 coatings, showing 99.99% antibacterial efficiency against *E. coli*. The results of osteoblastic cell proliferation confirmed the cytocompatibility of the HAp/ZIF-8@Gent coating. The ZIF-8@Gent coating, with excellent antibacterial activity and acceptable cytocompatibility, offers a promising new approach to mitigating implant-associated infections.

Author Contributions: Conceptualization, R.J., K.L. and X.Z.; methodology, R.J., J.L. and Y.D.; validation, R.J., K.L. and D.Y.; formal analysis, R.J.; investigation, R.J.; data curation, R.J.; writing—original draft preparation, R.J.; writing—review and editing, K.L., X.Z. and G.Y.; project administration, K.L. and X.Z.; funding acquisition, K.L. All authors have read and agreed to the published version of the manuscript.

Funding: This research was funded by the National Natural Science Foundation of China (Grant No. 51971236, 51502328), the Shanghai Rising-Star Program (Grant No. 21QA1410400), the Science and Technology Commission of Shanghai Municipality (Grant No. 21S31901200), and the Youth Innovation Promotion Association of the Chinese Academy of Sciences (Grant No. 2020254).

Institutional Review Board Statement: Not applicable.

Informed Consent Statement: Not applicable.

Data Availability Statement: Data are contained within the article.

Conflicts of Interest: The authors declare no conflicts of interest.

References

1. Li, K.; Liu, S.; Hu, T.; Razanau, I.; Wu, X.; Ao, H.; Huang, L.; Xie, Y.; Zheng, X. Optimized nanointerface engineering of micro/nanostructured titanium implants to enhance cell-nanotopography interactions and osseointegration. *ACS Biomater. Sci. Eng.* **2020**, *6*, 969–983. [CrossRef] [PubMed]
2. Geetha, M.; Singh, A.K.; Asokamani, R.; Gogia, A.K. Ti based biomaterials, the ultimate choice for orthopaedic implants—A review. *Prog. Mater Sci.* **2009**, *54*, 397–425. [CrossRef]
3. Liu, X.; Chu, P.K.; Ding, C. Surface modification of titanium, titanium alloys, and related materials for biomedical applications. *Mater. Sci. Eng. R Rep.* **2004**, *47*, 49–121. [CrossRef]
4. Liu, X.; Li, M.; Zhu, Y.; Yeung, K.W.K.; Chu, P.K.; Wu, S. The modulation of stem cell behaviors by functionalized nanoceramic coatings on Ti-based implants. *Bioact. Mater.* **2016**, *1*, 65–76. [CrossRef] [PubMed]
5. Legeros, R.Z. Calcium phosphate-based osteoinductive materials. *Chem. Rev.* **2008**, *108*, 4742–4753. [CrossRef]
6. Yook, H.; Hwang, J.; Yeo, W.S.; Bang, J.; Kim, J.; Kim, T.Y.; Choi, J.S.; Han, J.W. Design strategies for hydroxyapatite-based materials to enhance their catalytic performance and applicability. *Adv. Mater.* **2022**, *35*, 2204938. [CrossRef] [PubMed]
7. Wu, S.; Liu, X.; Gao, C. Role of adsorbed proteins on hydroxyapatite-coated titanium in osteoblast adhesion and osteogenic differentiation. *Sci. Bull.* **2015**, *60*, 691–700. [CrossRef]
8. Zheng, X.; Huang, M.; Ding, C. Bond strength of plasma-sprayed hydroxyapatite/Ti composite coatings. *Biomaterials* **2000**, *21*, 841–849. [CrossRef] [PubMed]
9. Arciola, C.R.; Campoccia, D.; Montanaro, L. Implant infections: Adhesion, biofilm formation and immune evasion. *Nat. Rev. Microbiol.* **2018**, *16*, 397–409. [CrossRef]
10. Filipović, U.; Dahmane, R.G.; Ghannouchi, S.; Zore, A.; Bohinc, K. Bacterial adhesion on orthopedic implants. *Adv. Colloid Interface Sci.* **2020**, *283*, 102228. [CrossRef]
11. Amin Yavari, S.; Castenmiller, S.M.; Van Strijp, J.A.G.; Croes, M. Combating implant infections: Shifting focus from bacteria to host. *Adv. Mater.* **2020**, *32*, 2002962. [CrossRef] [PubMed]
12. Wang, Y.; Teng, W.; Zhang, Z.; Zhou, X.; Ye, Y.; Lin, P.; Liu, A.; Wu, Y.; Li, B.; Zhang, C.; et al. A trilogy antimicrobial strategy for multiple infections of orthopedic implants throughout their life cycle. *Bioact. Mater.* **2021**, *6*, 1853–1866. [CrossRef] [PubMed]
13. Wang, Y.; Wang, F.; Zhang, H.; Yu, B.; Cong, H.; Shen, Y. Antibacterial material surfaces/interfaces for biomedical applications. *Appl. Mater. Today* **2021**, *25*, 101192. [CrossRef]
14. Predoi, D.; Iconaru, S.L.; Predoi, M.V.; Buton, N.; Motelica-Heino, M. Zinc doped hydroxyapatite thin films prepared by sol–gel spin coating procedure. *Coatings* **2019**, *9*, 156. [CrossRef]
15. Predoi, D.; Popa, C.L.; Chapon, P.; Groza, A.; Iconaru, S.L. Evaluation of the antimicrobial activity of different antibiotics enhanced with silver-doped hydroxyapatite thin films. *Materials* **2016**, *9*, 778. [CrossRef] [PubMed]
16. Hu, C.; Guo, J.; Qu, J.; Hu, X. Efficient destruction of bacteria with Ti(iv) and antibacterial ions in co-substituted hydroxyapatite films. *Appl. Catal. B* **2007**, *73*, 345–353. [CrossRef]
17. Troyano, J.; Carné-Sánchez, A.; Avci, C.; Imaz, I.; Maspoch, D. Colloidal metal–organic framework particles: The pioneering case of ZIF-8. *Chem. Soc. Rev.* **2019**, *48*, 5534–5546. [CrossRef] [PubMed]
18. Pettinari, C.; Pettinari, R.; Di Nicola, C.; Tombesi, A.; Scuri, S.; Marchetti, F. Antimicrobial MOFs. *Coord. Chem. Rev.* **2021**, *446*, 214121. [CrossRef]
19. Yan, L.; Gopal, A.; Kashif, S.; Hazelton, P.; Lan, M.; Zhang, W.; Chen, X. Metal organic frameworks for antibacterial applications. *Chem. Eng. J.* **2022**, *435*, 134975. [CrossRef]
20. Taheri, M.; Ashok, D.; Sen, T.; Enge, T.G.; Verma, N.K.; Tricoli, A.; Lowe, A.; Nisbet, R.D.; Tsuzuki, T. Stability of ZIF-8 nanopowders in bacterial culture media and its implication for antibacterial properties. *Chem. Eng. J.* **2021**, *413*, 127511. [CrossRef]
21. Lv, C.; Kang, W.; Liu, S.; Yang, P.; Nishina, Y.; Ge, S.; Bianco, A.; Ma, B. Growth of ZIF-8 nanoparticles in situ on graphene oxide nanosheets: A multifunctional nanoplatform for combined ion-interference and photothermal therapy. *ACS Nano* **2022**, *16*, 11428–11443. [CrossRef] [PubMed]
22. Zheng, H.; Zhang, Y.; Liu, L.; Wan, W.; Guo, P.; Nyström, A.M.; Zou, X. One-pot synthesis of metal–organic frameworks with encapsulated target molecules and their applications for controlled drug delivery. *J. Am. Chem. Soc.* **2016**, *138*, 962–968. [CrossRef] [PubMed]
23. Wang, L.; Liu, S.; Ren, C.; Xiang, S.; Li, D.; Hao, X.; Ni, S.; Chen, Y.; Zhang, K.; Sun, H. Construction of hollow polydopamine nanoparticle based drug sustainable release system and its application in bone regeneration. *Int. J. Oral Sci.* **2021**, *13*, 27. [CrossRef] [PubMed]
24. Chen, W.; Yun, F.; Zheng, S.; Shi, C.; Han, J. In situ growth ZIF-8 on porous chitosan/hydroxyapatite composite fibers for ultra-efficiently eliminating lead ions in wastewater. *Mater. Today Commun.* **2023**, *37*, 107255. [CrossRef]
25. Foroutan, R.; Jamaleddin Peighambardoust, S.; Amarzadeh, M.; Kiani Korri, A.; Sadat Peighambardoust, N.; Ahmad, A.; Ramavandi, B. Nickel ions abatement from aqueous solutions and shipbuilding industry wastewater using ZIF-8-chicken beak hydroxyapatite. *J. Mol. Liq.* **2022**, *356*, 119003. [CrossRef]

26. Predoi, S.A.; Ciobanu, S.C.; Chifiriuc, C.M.; Iconaru, S.L.; Predoi, D.; Negrila, C.C.; Marinas, I.C.; Raaen, S.; Rokosz, K.; Motelica-Heino, M. Sodium bicarbonate-hydroxyapatite used for removal of lead ions from aqueous solution. *Ceram. Int.* **2024**, *50*, 1742–1755. [CrossRef]
27. Jing, N.; Zhou, A.-N.; Xu, Q.-H. The synthesis of super-small nano hydroxyapatite and its high adsorptions to mixed heavy metallic ions. *J. Hazard. Mater.* **2018**, *353*, 89–98. [CrossRef] [PubMed]
28. Shang, S.; Zhao, Q.; Zhang, D.; Sun, R.; Tang, Y. Molecular dynamics simulation of the adsorption behavior of two different drugs on hydroxyapatite and zn-doped hydroxyapatite. *Mater. Sci. Eng. C* **2019**, *105*, 110017. [CrossRef]
29. Xue, W.; Liu, X.; Zheng, X.; Ding, C. In vivo evaluation of plasma-sprayed wollastonite coating. *Biomaterials* **2005**, *26*, 3455–3460. [CrossRef]
30. Xiao, Y.; Rong, L.; Wang, B.; Mao, Z.; Xu, H.; Zhong, Y.; Zhang, L.; Sui, X. A light-weight and high-efficacy antibacterial nanocellulose-based sponge via covalent immobilization of gentamicin. *Carbohydr. Polym.* **2018**, *200*, 595–601. [CrossRef]
31. Alfaro-Viquez, E.; Esquivel-Alvarado, D.; Madrigal-Carballo, S.; Krueger, C.G.; Reed, J.D. Antimicrobial proanthocyanidin-chitosan composite nanoparticles loaded with gentamicin. *Int. J. Biol. Macromol.* **2020**, *162*, 1500–1508. [CrossRef] [PubMed]
32. Rapacz-Kmita, A.; Bućko, M.M.; Stodolak-Zych, E.; Mikołajczyk, M.; Dudek, P.; Trybus, M. Characterisation, in vitro release study, and antibacterial activity of montmorillonite-gentamicin complex material. *Mater. Sci. Eng. C* **2017**, *70*, 471–478. [CrossRef] [PubMed]
33. Fischer, D.; Von Mankowski, A.; Ranft, A.; Vasa, S.K.; Linser, R.; Mannhart, J.; Lotsch, B.V. ZIF-8 films prepared by femtosecond pulsed-laser deposition. *Chem. Mater.* **2017**, *29*, 5148–5155. [CrossRef]
34. Choi, E.; Lee, J.; Kim, Y.-J.; Kim, H.; Kim, M.; Hong, J.; Kang, Y.C.; Koo, C.M.; Kim, D.W.; Kim, S.J. Enhanced stability of $Ti_3C_2T_x$ mxene enabled by continuous ZIF-8 coating. *Carbon* **2022**, *191*, 593–599. [CrossRef]
35. Castaldi, P.; Santona, L.; Enzo, S.; Melis, P. Sorption processes and xrd analysis of a natural zeolite exchanged with Pb^{2+}, Cd^{2+} and Zn^{2+} cations. *J. Hazard. Mater.* **2008**, *156*, 428–434. [CrossRef] [PubMed]
36. Zhu, Z.; Wu, Y.; Hu, C.; Zhang, L.; Ding, H.; Zhu, Y.; Fan, Y.; Deng, H.; Zhou, X.; Tang, S. Elimination of zinc ions from aqueous solution by a hydroxylapatite-biochar composite material with the hierarchical porous microstructures of sugarcane waste. *J. Clean. Prod.* **2022**, *362*, 132483. [CrossRef]
37. Van Rijt MM, J.; Nooteboom, S.W.; Van Der Weijden, A.; Noorduin, W.L.; De With, G. Stability-limited ion-exchange of calcium with zinc in biomimetic hydroxyapatite. *Mater. Des.* **2021**, *207*, 109846. [CrossRef]
38. Zhang, Y.; Zhu, J.; Li, S.; Xiao, Y.; Zhan, Y.; Wang, X.; Au, C.-T.; Jiang, L. Rational design of highly H_2O- and CO_2-tolerant hydroxyapatite-supported Pd catalyst for low-temperature methane combustion. *Chem. Eng. J.* **2020**, *396*, 125225. [CrossRef]
39. Zhang, L.; Yang, Y.; Xiong, Y.-H.; Zhao, Y.-Q.; Xiu, Z.; Ren, H.-M.; Zhang, K.; Duan, S.; Chen, Y.; Xu, F.-J. Infection-responsive long-term antibacterial bone plates for open fracture therapy. *Bioact. Mater.* **2023**, *25*, 1–12. [CrossRef] [PubMed]
40. Gaur, N.; Patenall, B.L.; Ghimire, B.; Thet, N.T.; Gardiner, J.E.; Le Doare, K.E.; Ramage, G.; Short, B.; Heylen, R.A.; Williams, C.; et al. Cold atmospheric plasma-activated composite hydrogel for an enhanced and on-demand delivery of antimicrobials. *ACS Appl. Mater. Interfaces* **2023**, *15*, 19989–19996. [CrossRef]
41. Wang, D.; Wu, Q.; Ren, X.; Niu, M.; Ren, J.; Meng, X. Tunable zeolitic imidazolate framework-8 nanoparticles for biomedical applications. *Small Methods* **2023**, *2023*, 2301270. [CrossRef]
42. Wajda, A.; Goldmann, W.H.; Detsch, R.; Boccaccini, A.R.; Sitarz, M. Influence of zinc ions on structure, bioactivity, biocompatibility and antibacterial potential of melt-derived and gel-derived glasses from CaO-SiO_2 system. *J. Non-Cryst. Solids* **2019**, *511*, 86–99. [CrossRef]
43. Xiang, Y.; Mao, C.; Liu, X.; Cui, Z.; Jing, D.; Yang, X.; Liang, Y.; Li, Z.; Zhu, S.; Zheng, Y.; et al. Rapid and superior bacteria killing of carbon quantum dots/ZnO decorated injectable folic acid-conjugated pda hydrogel through dual-light triggered ros and membrane permeability. *Small* **2019**, *15*, 1900322. [CrossRef] [PubMed]
44. Wu, Q.; Li, M.; Tan, L.; Yu, J.; Chen, Z.; Su, L.; Ren, X.; Fu, C.; Ren, J.; Li, L.; et al. A tumor treatment strategy based on biodegradable BSA@ZIF-8 for simultaneously ablating tumors and inhibiting infection. *Nanoscale Horiz.* **2018**, *3*, 606–615. [CrossRef]
45. Vasile, B.S.; Oprea, O.; Voicu, G.; Ficai, A.; Andronescu, E.; Teodorescu, A.; Holban, A. Synthesis and characterization of a novel controlled release zinc oxide/gentamicin–chitosan composite with potential applications in wounds care. *Int. J. Pharm.* **2014**, *463*, 161–169. [CrossRef] [PubMed]
46. Zhang, J.; Tan, W.; Li, Q.; Liu, X.; Guo, Z. Preparation of cross-linked chitosan quaternary ammonium salt hydrogel films loading drug of gentamicin sulfate for antibacterial wound dressing. *Mar. Drugs* **2021**, *19*, 479. [CrossRef] [PubMed]
47. Monteiro, N.; Martins, M.; Martins, A.; Fonseca, N.A.; Moreira, J.N.; Reis, R.L.; Neves, N.M. Antibacterial activity of chitosan nanofiber meshes with liposomes immobilized releasing gentamicin. *Acta Biomater.* **2015**, *18*, 196–205. [CrossRef] [PubMed]
48. Tao, B.; Zhao, W.; Lin, C.; Yuan, Z.; He, Y.; Lu, L.; Chen, M.; Ding, Y.; Yang, Y.; Xia, Z.; et al. Surface modification of titanium implants by ZIF-8@Levo/LBL coating for inhibition of bacterial-associated infection and enhancement of in vivo osseointegration. *Chem. Eng. J.* **2020**, *390*, 124621. [CrossRef]
49. Shahed, C.A.; Ahmad, F.; Günister, E.; Foudzi, F.M.; Ali, S.; Malik, K.; Harun WS, W. Antibacterial mechanism with consequent cytotoxicity of different reinforcements in biodegradable magnesium and zinc alloys: A review. *J. Magnes. Alloys* **2023**, *11*, 3038–3058. [CrossRef]

50. Chen, Z.; Liu, X.; Cheng, Z.; Tan, X.; Xiang, Y.; Li, J.; Zhang, Y.; Lu, Z.; Kang, E.-T.; Xu, L.; et al. Degradation behavior, biocompatibility and antibacterial activity of plasma electrolytic oxidation treated zinc substrates. *Surf. Coat. Technol.* **2023**, *455*, 129234. [CrossRef]
51. *ISO 10993.5*; Biological Evaluation of Medical Devices—Part 5: Tests for In Vitro Cytotoxicity. International Organization for Standardization: Geneva, Switzerland, 2009.